# Traffic jams and shocks of molecular motors inside cellular protrusions

I. Pinkoviezky and N. S. Gov*

*Department of Chemical Physics, Weizmann Institute of Science, P. O. Box 26, Rehovot 76100, Israel*

(Received 25 August 2013; revised manuscript received 3 March 2014; published 12 May 2014)

Molecular motors are involved in key transport processes inside actin-based cellular protrusions. The motors carry cargo proteins to the protrusion tip which participate in regulating the actin polymerization and play a key role in facilitating the growth and formation of such protrusions. It is observed that the motors accumulate at the tips of cellular protrusions and form aggregates that are found to drift towards the protrusion base at the rate of actin treadmilling. We present a one-dimensional driven lattice model, where motors become inactive after delivering their cargo at the tip, or by loosing their cargo to a cargoless neighbor. The results suggest that the experimental observations may be explained by the formation of traffic jams that form at the tip. The model is solved using a novel application of mean-field and shock analysis. We find a new class of shocks that undergo intermittent collapses. Extensions with attachment and detachment events and relevance to experiments are briefly described.

DOI: 10.1103/PhysRevE.89.052703 PACS number(s): 87.10.−e, 64.60.De, 87.15.−v

## I. INTRODUCTION

The traffic of molecular motors is an example of a nonequilibrium process [1–3]. A molecular motor convert the energy released from ATP hydrolysis into mechanical work. In this work we focus on the traffic of many molecular motors inside actin-based cellular protrusions, such as filopodia and stereocilia. These protrusions are of a few microns in length and fractions of microns in diameter, and contain a polarized bundle of actin filaments [4]. The actin polymerizes at the protrusion tip, such that it provides the force for the protrusion initiation, and treadmills at a constant rate when the protrusion reaches a steady-state shape. The motors move towards the tip and the actin treadmilling results in a motion towards the base [see Fig. 1(a) for an illustration].

Unconventional myosins bind and move processively toward the protrusion tip on these filaments (except for myosin-VI), as shown in Fig. 1(a). Experiments analyzing myosin traffic revealed that motors accumulate over a finite length scale at the tips of protrusions of different lengths [5]. A striking phenomenon is seen in a variety of experiments with different types of myosin motors [6–8]: The traffic of motors exhibit wave-trains, or "pulses" of aggregates of motors, that originate at the tip and move towards the base of the protrusion (opposite to the motors' active motion). The velocity of these aggregates is found to be close to that of the actin treadmilling, suggesting that these are inactive or jammed motors. The theoretical challenge for a successful model is to explain both the finite length of the accumulation of motors at the tips and to provide a mechanism for the counterpropagating aggregates of motors.

The simplest description of motors along a single linear track is in terms of a total asymmetric exclusion process (TASEP) [3]. We can model a protrusion as a half closed tube, open at its base to the cell cytoplasm [Fig. 1(a)]. Several works have dealt with this boundary condition together with attachment and detachment kinetics of the motors to the tracks [9–11]. These models find that at steady state the tubes are practically all jammed, and longer tubes have longer jammed regions, in contrast with the observations for cellular protrusions. In Ref. [12] it was shown that a track coupled to an infinite reservoir [illustrated in Fig. 2(a)] produces an accumulation with a fixed length for different system sizes [see Fig. 2(b)]. This is implemented by coupling TASEP with Langmiur kinetics (LK). However, it is unlikely that the confined volume of a cellular protrusion can serve as an infinite reservoir.

Similarly, the properties of the observed aggregates of motors do not fit the traffic jams arising in TASEP. For example, it seems from experiments that the aggregates originate only at the protrusion tips, are rather stable while propagating, and have low-density regions between them. This is not what happens in TASEP where jams appear at the high-density (HD) phase [13], and jams appear everywhere. Sparse jams between free-flow regions appear in models of vehicular traffic [14], but they result from the combination of synchronous update and several particle velocities. There is no obvious reason why this should apply for molecular motors traffic. Therefore, we present a new model, based on a generalization of TASEP with half closed boundary conditions, that may explain the observed phenomena of motor aggregates.

The paper plan is as follows. In the next section we present the model. In Sec. III we present the calculation for the simplified model, while in Sec. IV we present the results for this model. Section V is dedicated to describing briefly the results of incorporating attachment and detachment events to the simplified model. Finally we conclude the paper in Sec. VI.

## II. MODEL

To explain the observed phenomena we consider a generalization of TASEP as described in Fig. 1(b). While the core of cellular protrusions contain a bundle of actin filaments, we use a coarse-grained description of a single track for simplicity. Each particle correspond to a molecular motor and can be in one of two states: "inactive" where it is immobile on the actin track, and "active" where it can hop unidirectionally only when the next site is empty. We note that internal degree of

*nir.gov@weizmann.ac.il

 

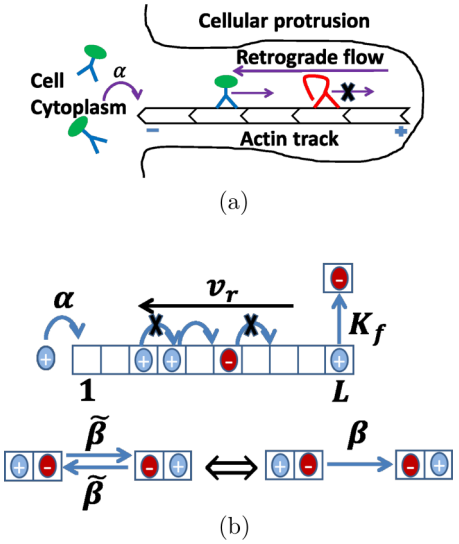


FIG. 1. (Color online) (a) An illustration of a cellular protrusion. Myosin motors enter with probability $\alpha dt$ from the cell's cytoplasm. They move on the actin track. Green ellipses are cargoes, and without it the tail folds to inhibit the motor domain. (b) The model. Particles enter the first site with probability $\alpha dt$ and "switch off" only at the last site; there is no exit from the right. The track itself moves backward with probability $v_r dt$. Particles can exchange their mobility state with rate $\tilde{\beta}$ in a process that can be mapped to a unidirectional process with rate $\beta$.

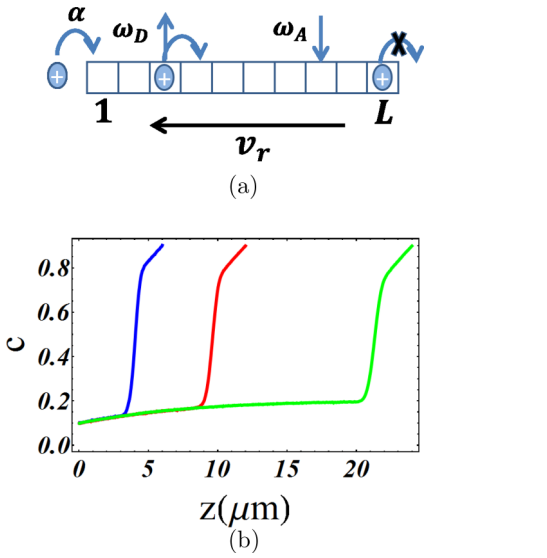


FIG. 2. (Color online) TASEP with Langmuir kinetics (LK): (a) Illustration of the process. Particles attach with a rate $\omega_A$ and detach with a rate $\omega_D$. The entrance rate is $\alpha$, and the exit rate on the right is zero. The track itself is moving backwards with a new site created on the right with a rate $v_r$. (b) Density profiles for $\alpha = 0.1, v_r = 0.1, \omega_A = 5 \times 10^{-4}, \omega_D = 2 \times 10^{-3}$, the size of a site $l = 30$ nm. System sizes ($\Delta z^0 = Ll$): $L = 200, \Delta z^0 = 6\,\mu$m (blue leftmost curve), $L = 400, \Delta z^0 = 12\,\mu$m (red middle curve), $L = 800, \Delta z^0 = 24\,\mu$m (green rightmost curve).

freedom was considered in the past [15–19]. Motivated by experiments and theoretical models, we propose the following properties for the dynamics of the activity state of the motors: It was found that several types of molecular motors become processive only when they are bound to a cargo molecule [20,21]. Since in many cases the cargo is involved in regulating the actin polymerization at the protrusion tip [8,22,23], we assume that the cargo can only detach from the motor there, due to a competing binding site for the cargo at the tip. Upon release of the cargo the motor becomes inactive. Note that the reverse process of releasing the cargo from the tip is neglected here since the cargo participates in chemical reactions related to the actin polymerization and is considered to be "consumed" in this process.

When inactive, motors may detach from the actin filament, or stay attached [20] and drift towards the protrusion base due to the actin treadmilling. Furthermore, neighboring motors can "steal" the cargo from each other [21], and this introduces a conservation of the activity whereby an inactive motor can only become active at the expense of an adjacent motor [Fig. 1(b)]. Since the cargo carried by the myosin motors is of single-molecule nature [8,20,23], it is unlikely that a single cargo can be bound simultaneously to several motors. Note that the cargo-swapping process is reversible (bidirectional) and does not involve the consumption of ATP (cargo swapping was previously considered in Ref. [24]). However, due to the underlying asymmetrical motion of the active motors, we find that this process is effectively rectified and can be mapped to a unidirectional process where the cargo is only transferred backwards between the motors [see Appendix A for details; Fig. 1(b)]. All the simulations in the paper were carried out with the bidirectional reactions and rates, while the analytical treatment is carried out with the unidirectional reaction. Such a unidirectional interaction is known to produce a robust traffic jam (condensate) [25].

We next extend our model to include attachment and detachment kinetics, in two forms. For completeness, and simplicity, we first extend the model to include LK. However, as noted above, the confined volume between the actin core and the surrounding membrane of the protrusion is very different from the infinite reservoir considered in LK [12]. We therefore also treat the case of exchange of motors between the actin track and a free diffusive space, which we implement as a symmetric random walk on a one-dimensional lattice without exclusion. We begin by considering the simplified model, which does not take into account attachment and detachment kinetics.

The parameters in the simplified model are the following: (1) $K_f dt$ is the probability for a particle to switch from active (+) to an inactive (−) state at the last site. (2) $\alpha dt$ is the probability that a particle enters the system at the left boundary. (3) $\tilde{\beta} dt$ is the probability that the cargo is swapped between adjacent inactive and active motors [Fig. 1(b)]. (4) $v_r$ is the rate at which a new site (actin monomer) is added at the right end, and simultaneously a site is removed at the left end. The actin treadmilling velocity is therefore $v_r$, and we maintain a constant overall length of the track. The treadmilling moves the track and all the motors towards the protrusion base with velocity $v_r$. (5) We normalize the probabilities such that $dt$ is the hopping probability of an active particle to a free site.

We show an example kymograph of the dynamics arising in our model in Fig. 3(a). We find that near the tip there is a region of accumulation of motors, and large traffic jams are

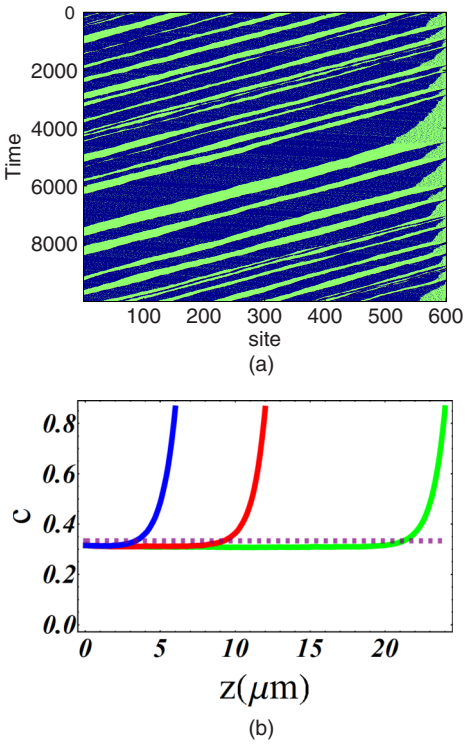


FIG. 3. (Color online) (a) Kymograph. Green (bright) points are active particles, while dark blue is the empty space. (b) Density profiles for systems of lengths $z = 6$, 12, and 24 $\mu$m. Data are for $\alpha = \beta = 0.05, v_r = 0.1$, and $K_f = 0.002$. The dashed purple curve is the theoretical bulk density $c_b$ [Eq. (10)]. The spatial extent of each site corresponds to a motor step (i.e., 30 nm), therefore $z = i \times 0.03\ \mu$m, where $i$ is the site number.

initiated there. Each traffic jam corresponds to an inactivation event of a motor at the tip. When a jam is formed, it transiently depletes the tip region, which gets refilled shortly afterwards. These properties of robust aggregates that form near the tip and deplete it correspond qualitatively with the experimental observations of myosin-X [6] and myosin-XV [7] in filopodia.

We find in Fig. 3(b) that the accumulation length of the motors near the tip is independent of the system size (as in the case with LK alone; Fig. 2). We stress that without the switching mechanism the track would be uniformly occupied with density $1 - v_r$ except for a shock at the left end. The jams initiated by the inactive particles determine a finite length of the accumulation region and do not let it grow to the system size. Such localized accumulations of motors are observed near the tips of stereocilia of different lengths [5], and our model suggests that this arises from the turnover of motors through the formation of jams.

The model with LK includes particle detachment with rate $\omega_D$ and particle attachment with rate $\omega_A$ (given that site $i$ is empty); see Fig. 4(a). To take into account the free diffusion in the tube we present the simplified model coupled to a diffusive track with symmetric hopping rate $D$ and without exclusion, as depicted in Fig. 4(b). Since a single myosin-X can walk the entire filopodium [26] we will consider the attachment and detachment probabilities to be small. Moreover, we do not take

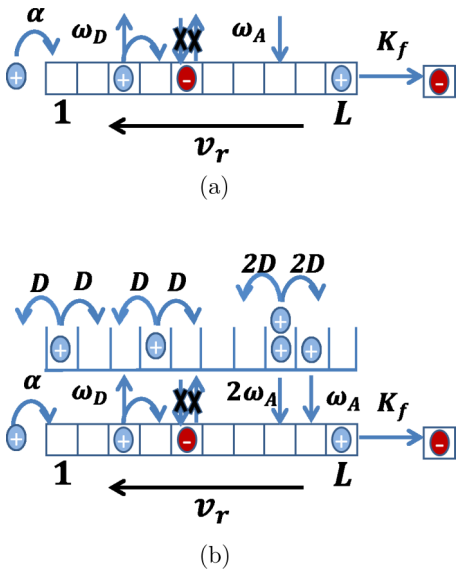


FIG. 4. (Color online) (a) Model with LK. The same interactions as in the simplified model. Particles can disappear with probability $\omega_D dt$ and appear with $\omega_A dt$. (b) Model with coupling to a diffusive track. Since there is no exclusion in the diffusive track the detachment kinetics from the active track are the same as in (a). The attachment probabilities to the active track are proportional to the occupancy in the diffusive track. The occupancies at the diffusive track sites are unlimited. At both processes described in (a) and (b) particles switch off at the tip and participate in cargo swapping with rate $\tilde{\beta}$.

into account detachment events of the inactive motors as it was suggested that these motors are at the prestroke conformation [20], which binds strongly to actin [27].

## III. CALCULATIONS IN THE SIMPLIFIED MODEL

We now turn to analyze the simplified model in detail, in steady state. The interesting behavior arises in the regime where the inactivation rate $K_f$ is small, and significant accumulation of motors occurs at the tip. In order to allow for analytic solutions, it is useful to choose the "mesoscopic scaling" $K_f = \frac{\Lambda_f}{L}$ [16] in the thermodynamic limit, and to use a spatial coordinate $x = \frac{i}{L}, 0 \leqslant x \leqslant 1$, where $L$ is the number of sites in the system. Furthermore, the reversible cargo-swapping process with rate $\tilde{\beta}$ is mapped to an effective unidirectional process with rate $\beta = \tilde{\beta}/(1 + \tilde{\beta})$ [see Appendix A; Fig. 1(b)], which we then use in the analytic

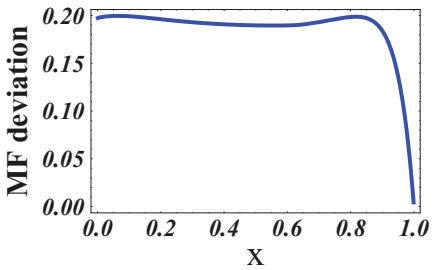


FIG. 5. (Color online) Deviation of MF approximation. Data are for $\alpha = \beta = 0.05, v_r = 0.1$, and $K_f = 0.002$.

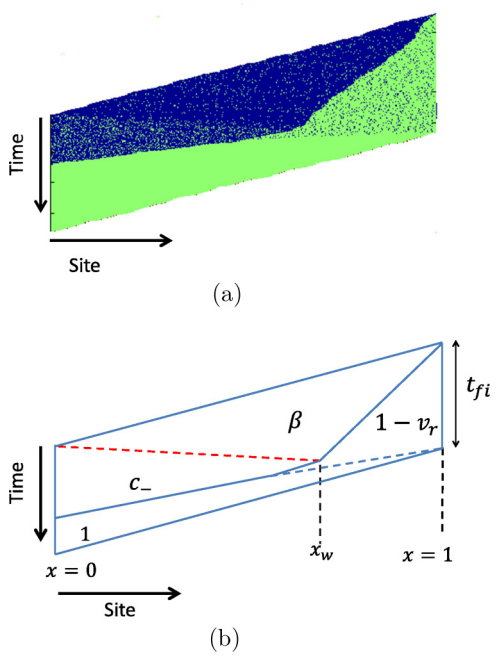


FIG. 6. (Color online) (a) An example of a parallelogram (or slice) for $\alpha = 0.2, \tilde{\beta} = 0.0523, v_r = 0.1$, and $\Lambda_f = 0.2$. (b) A description of a slice with the different density regions and the slopes connecting them. In both figures we see $x_w$ [Eq. (4)] where the densities $[c_-, \beta, 1-v_r]$ meet.

analysis. The average time between two successive switching off events is $\langle t_f \rangle = \frac{L}{\Lambda_f (1-v_r)}$ (where we take into account the density $1-v_r$ at the tip); therefore, in the following we renormalize $t_f$ by $L$ so $\langle t_f \rangle = \frac{1}{\Lambda_f (1-v_r)}$.

We start by comparing the numerical simulations to a naive mean-field approximation (MFA) [28], which fails, as demonstrated in Fig. 5. The reason for this deviation lies in the fact that the system separates into regions of different mean densities and currents. We therefore proceed with a detailed calculation of the *average* concentration profiles of the motors in our model, which is based on using a MFA within each distinct region. We divide the space-time evolution of the system into parallelogram slices as shown in Fig. 6(a). The $i$th parallelogram is defined by $t_{fi}$, the time between two successive inactivation events at the tip.

We find four regions of different average concentrations [Fig. 6(b)]: (1) HD region near the tip, with density $1-v_r$, (2) jammed regions of density 1, (3) free-flow regions with density $\beta$, and (4) the entrance region near the base with density $c_- = \min(\alpha, \frac{1-v_r}{2})$ as the system cannot transmit a density greater than the density of maximal current in the periodic system. Therefore, to get the density profile we need to average over the contributions of the different regions. Summing the density contributions from each slice and dividing it by the total time $T_{\text{tot}} = \sum t_{fi}$, we get

$$c(x) = \frac{(1-v_r)\sum t_{v_r i}(x) + \beta \sum t_{\beta i}(x) + c_- \sum t_{c_- i}(x) + \sum t_{Ji}(x)}{\sum t_{fi}}, \tag{1}$$

where $t_{v_r i}$ is the time a region with density $1-v_r$ have spent in $x$ in the $i$th slice, $t_{\beta i}$ is for density $\beta$, $t_{c_- i}$ is for density $c_-$, $t_{Ji}$ is for density 1, and the summation is over all parallelograms.

The lines separating these different regions have slopes that can be calculated according to the shock velocities [29]:

$$v_s = \frac{j_r - j_l}{c_r - c_l}, \tag{2}$$

where $j_{r,l}, c_{r,l}$ denote the current and density on the right and left side of the shock, respectively. The right direction is defined as the positive $x$ direction. In the following we take the currents for the different density regions to be given by the mean-field current: $j = c(x)[1 - c(x) - v_r]$. For example, the slope between the $1-v_r$ and $\beta$ densities is (see Fig. 7)

$$\begin{aligned} j_l &= \beta(1-\beta-v_r), \\ j_r &= (1-v_r)[1-(1-v_r)-v_r] = 0, \\ v_s &= \frac{0-\beta(1-\beta-v_r)}{1-v_r-\beta} = -\beta. \end{aligned} \tag{3}$$

Using these slopes, we calculate the time duration that each spatial point spends in a region of certain density and the locations where different densities meet.

One such important meeting point is between the regions of densities $[1-v_r, \beta, c_-]$, which if it exists defines the meeting between the regions influenced by both boundaries (Fig. 6). This point defines the location of the matching between the left and right solutions, given by

$$x_w = \frac{v_r(1-v_r-\beta-c_-)}{v_r(1-v_r-\beta-c_-) + \beta(1-c_-)}. \tag{4}$$

The second length scale is $x_{v_r i}$, which is the distance from $x=1$ to the "triple" point where the $1-v_r, \beta, 1$ regions meet. If $x_{v_r}$ exist, $x_w$ does not. Again, by examining the geometry of the slice we get for the $i$th slice [see Fig. 7(b)]

$$x_{v_r i} = \frac{\beta}{1-\beta} t_{fi}, \tag{5}$$

where $x_{1i}$ is the distance from $x=1$ to the point where $c_-, 1-v_r, 1$ meet. The length for the $i$th parallelogram is [see Fig. 8(b)]

$$x_{1i} = \frac{c_-}{1-c_-} t_{fi} + \frac{\beta - c_-}{\beta(1-c_-)}(1-x_w). \tag{6}$$

Another important length is $x_{\alpha i}$, which is the distance from $x=0$ to the point where the densities $c_-, 1, \beta$ meet [this is described in Fig. 8(c)]:

$$x_{\alpha i} = \frac{v_r(1-v_r-\beta-c_-)}{\beta(1-c_-)} x_{v_r i}. \tag{7}$$

We stress that all the lengths, except $x_w$, depend on the specific realization of the parallelogram; i.e., they depend on $t_{fi}$.

The calculation proceeds as follows. Let $i$ be an index of a parallelogram, and say we have a spatial point $x$. First,

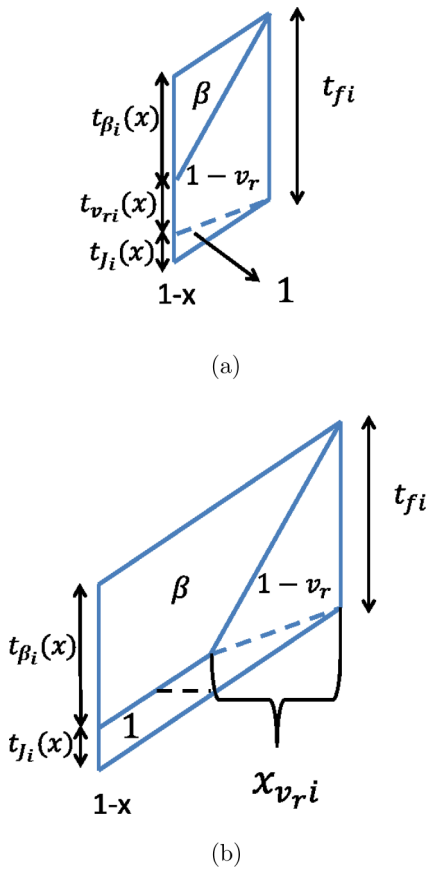


FIG. 7. (Color online) Contributions of parallelograms for $x > x_w$. The density of each region is shown. (a) $1-x < x_{v_r i}$ (b) $1-x > x_{v_r i}$. The black horizontal dashed line marks the size of the jammed area.

consider $x > x_w$. Each slice will have different contribution to the density. As seen from Fig. 7 the contribution depend on whether $1-x$ is greater than $x_{v_r i}$ or not. Therefore, we divide the set of slices into two subsets (see Fig. 7):

$$a = \{i | x_{v_r i} > 1-x\} \quad b = \{i | x_{v_r i} < 1-x\}$$

and then divide the sum on parallelograms to two sums:

$$\sum_i = \sum_{i\in a} + \sum_{i\in b}, \tag{8}$$

where at each sum we consider only parallelograms in the relevant subset.

Consider now $x < x_w$. We can now divide the set of all parallelograms into four subsets:

$$A = \{i | x_{1i} > 1-x\},$$
$$B = \{i | x_{1i} < 1-x, x_{v_r i} > 1-x_w\},$$
$$C_1 = \left\{i | \frac{\beta(1-c_-)}{v_r(1-v_r-\beta-c_-)}x < x_{v_r i} < 1-x_w\right\},$$
$$C_2 = \left\{i | x_{v_r i} < \frac{\beta(1-c_-)}{v_r(1-v_r-\beta-c_-)}x\right\}.$$

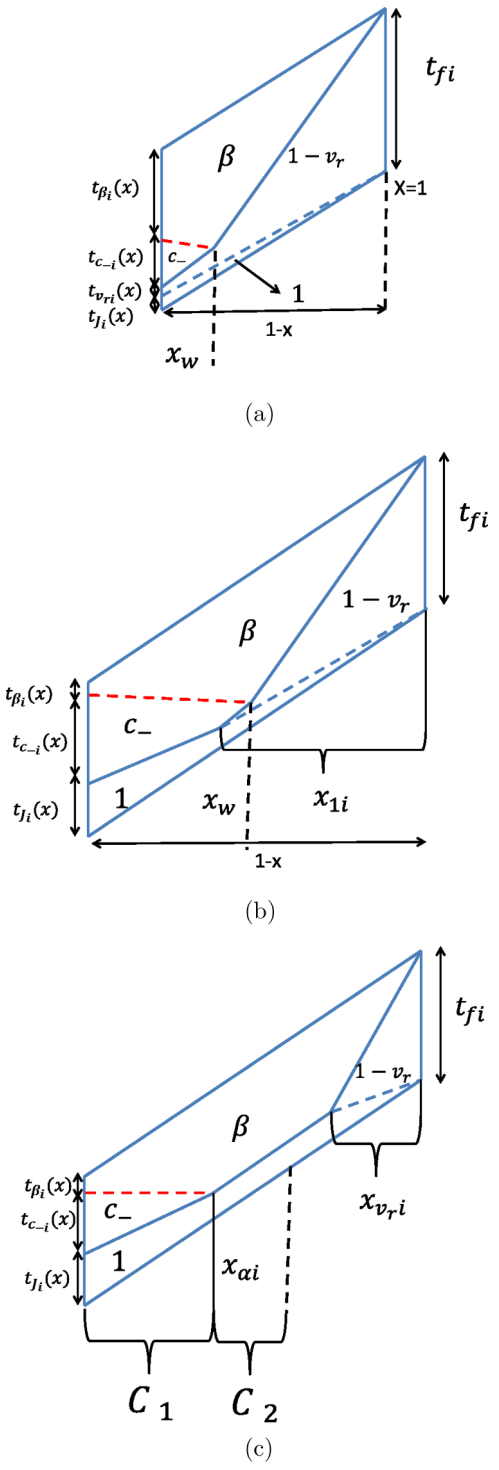


FIG. 8. (Color online) Contributions of parallelograms for $x < x_w$. (a) Slices that are in subset $A$. (b) The subset $B$. (c) The subsets $C_1, C_2$.

The contributions of slices of each subset are described in Fig. 8. For each spatial point $x$ we divide the parallelograms to four sums:

$$\sum_i = \sum_{i\in A} + \sum_{i\in B} + \sum_{i\in C_1} + \sum_{i\in C_2}. \tag{9}$$

We denote conditional mean of a random variable $V$ on the subset $\Gamma$ (i.e., not averaging over all space but only on the given subset) as $\langle V|\Gamma\rangle$. Mathematically, it is defined as

$$\langle V|\Gamma\rangle = \int_{\Gamma} V P(V|\Gamma)\, dV,$$

where $P(V|\Gamma)$ is the conditional probability distribution function. We give the expressions for the conditional means $\langle x_{v_r i}|a\rangle, \langle x_{v_r i}|b\rangle, \langle t_f|A\rangle, \langle x_{1i}|B\rangle, \langle x_{v_r i}|C_1\rangle$, and $\langle x_{v_r i}|C_2\rangle$ in Appendix B.

We give the details of the calculation in Appendix C. The general scheme is as follows. We calculate the sums in the numerator of Eq. (1). The time interval of a given density depend on $x$ as given by the shock velocities (which are the slopes between the different regions). We divide the sums to sums over different subsets [as in Eqs. (8) and (9)]. At each subset we have information on the inactivation time difference for the parallelogram. Therefore, the averages that appear in the expression should be conditioned with respect to the subset (expressions are found in Appendix B).

## IV. RESULTS FOR THE SIMPLIFIED MODEL

### A. Density profile

The density profile that we get from Sec. III and Appendix C is

$$\begin{aligned} x > x_w : c(x) &= \frac{\beta}{\beta+v_r} + \left(1 - v_r - \frac{\beta}{\beta+v_r}\right) \exp\left(\frac{x-1}{\xi_r}\right); \\ x < x_w : c(x) &= \frac{\beta}{\beta+v_r} + \frac{v_r(c_- - \beta)}{(c_- + v_r)(\beta+v_r)} \exp\left(-\frac{x}{\xi_l}\right) + \left(1 - c_- - \frac{c_-}{c_- + v_r}\right) \\ &\quad \times \exp\left[\frac{\Lambda_f(1-v_r)(c_- - \beta)}{c_-\beta}(x_w - 1)\right] \exp\left[\frac{\Lambda_f(1-v_r)(1-c_-)}{c_-}(x-1)\right], \end{aligned} \tag{10}$$

where

$$\xi_r = \frac{\beta}{\Lambda_f(1-\beta)(1-v_r)}, \quad \xi_l = \frac{v_r(1-v_r-\beta-c_-)}{\Lambda_f(1-c_-)(1-v_r)(1-\beta)}, \tag{11}$$

where $\xi_l, \xi_r$ are the "healing" lengths of the left and right exponentials, respectively, as shown in Figs. 9(b)–9(d). We see that the solution is composed of two parts, the "right" solution controlled by the right boundary condition and the "left" solution controlled by the left boundary condition.

The agreement between the simulations and the calculated density profile [Eq. (10)] is very good and improves for large systems $L \to \infty$. For comparison, we also denote the bulk density predicted from the periodic model [25] with treadmilling: $c_b = \beta/(\beta + v_r)$, as seen in Eq. (10).

### B. Jam size distribution

The black horizontal dashed line in Fig. 7(b) represents the jam size in a time slice. From considering the geometry of a slice we see that the jam size is an exponential random variable with mean value

$$\langle \Omega \rangle = L \frac{\beta}{\Lambda_f} \frac{1 - v_r - \beta}{(1-v_r)(1-\beta)}. \tag{12}$$

We compare this result with simulation results in Fig. 10, and we see that the two agree very well.

### C. Phase diagram

The phase diagram of the system is shown in Fig. 9. We first note that for $\beta = 1 - v_r$, both the mean jam size [Eq. (12)] and the exponential accumulation at the tip [Eq. (10)] vanish. For $\beta > 1 - v_r$ we indeed find that the system exhibit only regular TASEP jams, and it behaves as TASEP with treadmilling velocity $v_r$ and zero current [Fig. 9(a)].

This transition can be understood in terms of the velocities of the holes entering the system at the tip. This is the same condition as in the periodic system [25] where instead of global density, $1 - v_r$ is the local density at the tip. If $1 - v_r$ is the local density at the right end, it is also the average velocity of the holes. Now, consider the impurity particle as a defect hole. This defect hole has a velocity $\beta$. If the average hole velocity is greater than the defect velocity, i.e., $1 - v_r > \beta$, the motion of the holes is limited by this defect. This limitation forms a region with no holes (as holes cannot pass the defect hole); i.e., it forms a condensate which is the traffic jam.

Next, we note that $x_w$ becomes negative when $1 - v_r - c_- < \beta$, which corresponds to a vanishing of the left exponential in $c(x)$, and therefore this phase is denoted as Jams-R [Fig. 9, and profile (b)]. Finally for positive $x_w$ (denoted as the Jams-LR phase in Fig. 9) we find that for $\alpha > \beta$ jams grow as they approach the base [near the left end, Fig. 9(c)], while for $\alpha < \beta$ they shrink [Fig. 9(d)]. This means that for $\alpha < \beta$ there is a profile with a step located at $x_w$.

### D. Shocks

Taking the limit of $\alpha \to 0$ by using the scaling $\alpha \sim 1/L$ and $L \to \infty$ we get from Eq. (10)

$$\begin{aligned} &\mathbf{x > x_w}: \\ &c(x) = \frac{\beta}{\beta+v_r} + \left(1 - v_r - \frac{\beta}{\beta+v_r}\right) \\ &\qquad \times \exp\left[\frac{\Lambda_f(1-v_r)(1-\beta)}{\beta}(x-1)\right]; \\ &\mathbf{x < x_w}: \\ &c(x) = \frac{\beta}{\beta+v_r} - \frac{\beta}{\beta+v_r} \\ &\qquad \times \exp\left[-\frac{\Lambda_f(1-\beta)(1-v_r)}{v_r(1-v_r-\beta)}x\right]; \end{aligned} \tag{13}$$

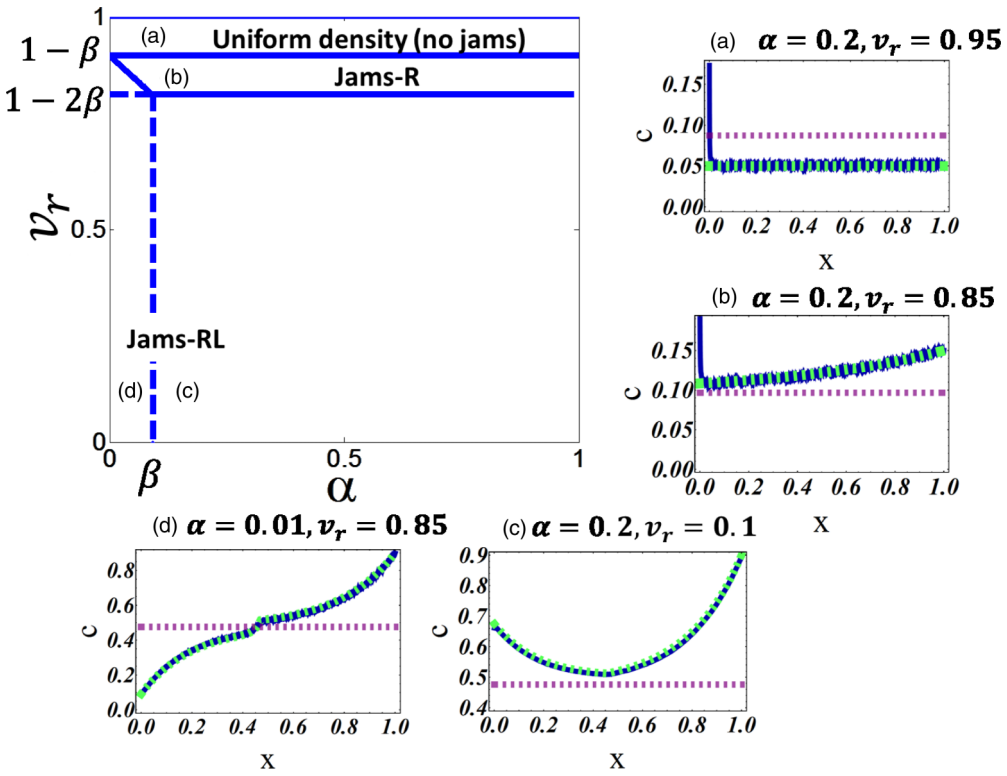


FIG. 9. (Color online) Phase diagram in $(\alpha, v_r)$ space and typical density profiles, using $\tilde{\beta} = 0.1, \beta = 0.0909$. $v_r > 1-\beta$: Uniform density phase (no jams), with density profile (1). $1-\beta > v_r > 1-\beta-c_-$: Jams-R phase where the behavior is dominated by the right boundary alone (density profile b). $1-\beta-c_- > v_r$: Jams-LR phase where the behavior is influenced by both boundaries. The dashed vertical line separates this phase into two regions: (c) $\alpha > \beta$ and (d) $\alpha < \beta$. The inactivations rates were chosen as (a) $\Lambda_f = 0.5$, (b) $\Lambda_f = 1$, (c) $\Lambda_f = 0.5$, (d) $\Lambda_f = 0.5$. Density profiles: Blue curves = simulation results; green dashed curves = theoretical result of Eq. (10); horizontal dashed purple curves = bulk density $c_b$.

we see that the density profile is discontinuous at $x = x_w$, therefore it exhibit a localized shock. The discontinuity magnitude is

$$\begin{aligned}\Delta c &= c(x_w^+) - c(x_w^-) \\ &= (1-v_r)\exp\left[\frac{\Lambda_f(1-v_r)(1-\beta)}{\beta}(x_w - 1)\right] \\ &= (1-v_r)\exp\left[-\frac{\Lambda_f(1-v_r)(1-c_-)(1-\beta)}{v_r(1-v_r-\beta-c_-)+\beta(1-c_-)}\right].\end{aligned} \tag{14}$$

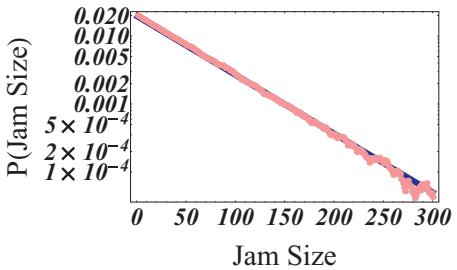


FIG. 10. (Color online) Jam size distribution for $\alpha = \beta = 0.05$, $v_r = 0.1, \Lambda_f = 1$. Blue curve is Eq. (12), while red light points are simulation data points.

We give an example for this kind of density profile in Fig. 11. We find that the location of the shock in the system has a reentrant behavior as a function of $v_r$ (Fig. 11), while the amplitude of the density discontinuity [$\Delta c$, Eq. (14)] is also nonmonotonic (Fig. 11).

Unlike previous shocks found in TASEP-like models [12,16,30,31] the shock we find is only defined for the *average* concentration, while it maintains a dynamic nature: it undergoes intermittent collapses (kymograph in Fig. 11). Furthermore, these shocks do not obey the usual Rankine-Hugoniot relation that follows from a naive MFA: $c(x_w^-) = 1 - c(x_w^+) - v_r$. During the time that no motor is switched off at the tip, there is an accumulation of particles, and a domain wall fulfilling the shock relation is established: $c(x_w^-) = 0, c(x_w^+) = 1 - v_r$, so that $\Delta c|_{x_w} = 1 - v_r$.

The probability that such a domain wall exists at any given time can be calculated by writing

$$\Delta c = (1-v_r)P_w, \tag{15}$$

and comparing it with Eq. (14) we get

$$\begin{aligned}P_w &= \frac{c(x_w^+) - c(x_w^-)}{1-v_r} \\ &= \exp\left[-\frac{\Lambda_f(1-v_r)(1-c_-)(1-\beta)}{v_r(1-v_r-\beta-c_-)+\beta(1-c_-)}\right],\end{aligned} \tag{16}$$

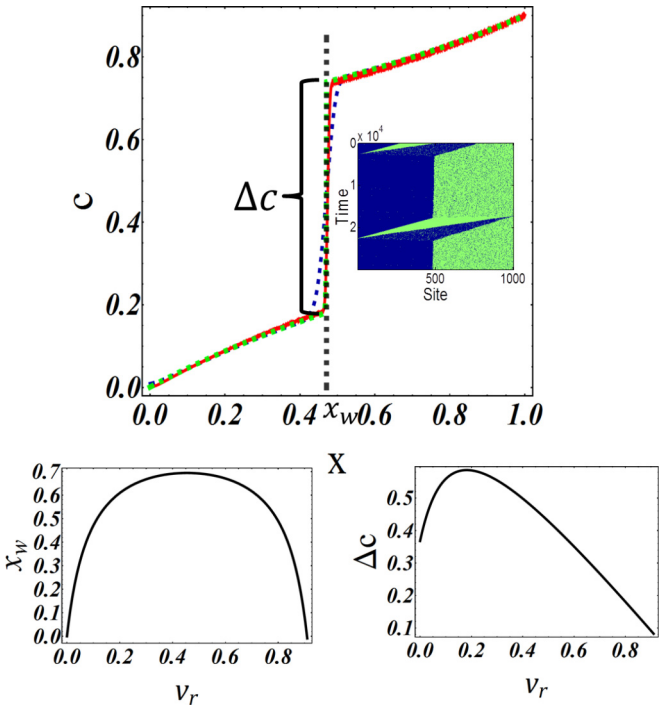


FIG. 11. (Color online) System exhibiting a shock: Density profile for $\alpha = 1/L, v_r = 0.1, \Lambda_f = 0.1$, and $\tilde{\beta} = 0.1, \beta = 0.0909$ with $L = 10^3$ (dashed dark blue curve) and $L = 10^4$ (red solid curve). Green dashed line is the theoretical result of Eq. (10). Vertical dashed line is $x_w$. Inset: Kymogrpah of the system. Bottom, left: The shock location $x_w$ from Eq. (4); right: the density jump at the shock [$\Delta c$, Eq. (S48)].

which is also the fraction of time duration that no jam is initiated at the tip.

## V. RESULTS FOR LANGMUIR KINETICS AND DIFFUSIVE TRACK

### A. Langmuir kinetics

We begin by incorporating Langmuir kinetics to the simplified model. As we noted in the introduction, this is not a realistic description of the system, yet it is the first step toward a more realistic description. This model is depicted in Fig. 4(a). We take the LK rates to be $\omega_{D/A} = \Omega_{D/A}/L, \Omega_{D/A} \sim O(1)$ such that a single motor is probable to have a run length of the entire system [26]. We show a kymograph and a density profile in Fig. 12(b). As in the simplified model, the system separates into jammed and free-flow regions, with the jams moving left while particles accumulate at the right end until a particle is switched off.

We can still describe the system as being composed of parallelograms. These slices in turn are composed of regions with different densities connected through shocks. Note, however, that now the shocks can be localized (i.e., $v_s = 0$) [12]. Furthermore, the system can exhibit two localized domain walls: one controlled by the entrance rate $\alpha$ and the other by $\beta$. The effective swapping rate can be considered as a second entrance rate as it induces a region with density $\beta$. To get the locations of the shocks one needs to repeat the

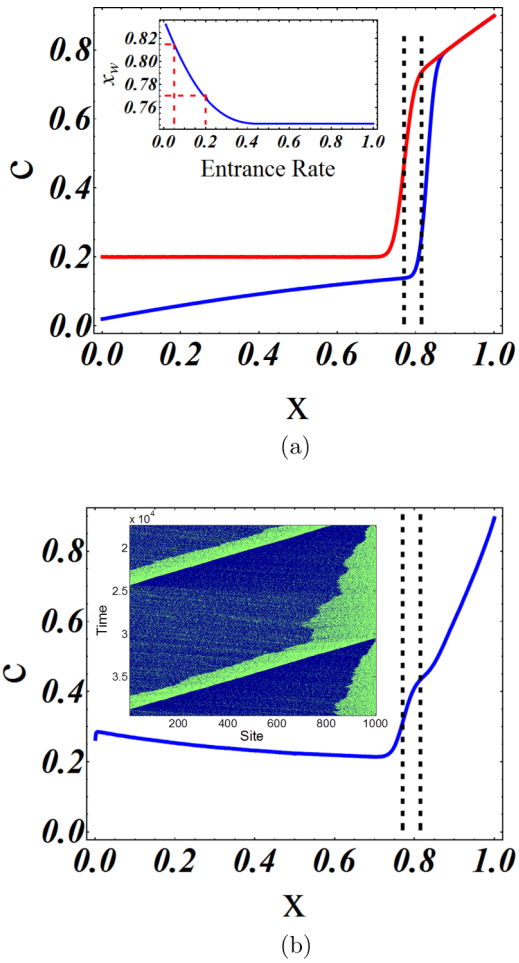


FIG. 12. (Color online) System with two LK shocks. (a) Density profiles for a system with LK but without switching off. Curves are for $\Omega_A = 0.2, \omega_D = 0.8, v_r = 0.1$ with $\alpha = 0.2$ (red left curve) and $\alpha = 0.02$ (blue right curve). Dashed vertical lines mark the locations of the shocks, corresponding to the two values of $\alpha$, as shown also in the inset. Inset: Location of the shock as a function of the entrance rate. Dashed lines correspond to the rates that match $\alpha$ and $\beta$ in (b). (b) Density profile for a system with $\Lambda_f = 0.1, \beta = 0.02$ ($\tilde{\beta} = 0.020408$), $\alpha = 0.2, \Omega_A = 0.2, \Omega_D = 0.8, v_r = 0.1$. Dashed vertical lines mark the locations of the shocks, as in (a). Inset: A kymograph demonstrating the two shocks.

calculation described in Ref. [32] with retrograde velocity $v_r$ and exit rate equal to zero. We describe the results briefly, as a similar calculation was carried out in detail in Ref. [32].

The locations of the shocks are given by

$$c_{\text{left}}(x_w) = 1 - v_r - c_{\text{right}}(x_w); \tag{17}$$

$c(x)$ is the solution of

$$\frac{dc}{dx}[1 - v_r - 2c(x)] = \Omega_D(K+1)\left[\frac{K}{K+1} - c(x)\right], \tag{18}$$

where $K = \Omega_A/\Omega_D$. It is convenient to transform to a new variable $\sigma(x)$:

$$\sigma(x) = \frac{1}{v_r + \frac{K-1}{K+1}}\left[2c(x) - 1 - \frac{K-1}{K+1}\right]. \tag{19}$$

With $\sigma$ as the new variable the solution to Eq. (18) takes the form of

$$|\sigma(x)|e^{\sigma(x)} = Y(x), \tag{20}$$

where $Y(x) = |\sigma(x_0)| \exp\{\Omega_D \frac{K+1}{v_r - \frac{1-K}{1+K}}(x - x_0) + \sigma(x_0)\}$. A convenient way to write the solution is

$$\begin{aligned} \sigma(x) &= W[Y(x)], \quad \sigma(x) > 0, \\ \sigma(x) &= W[-Y(x)], \quad \sigma(x) < 0, \end{aligned} \tag{21}$$

where $W$ is the Lambert W function [33]. The W function is a multivalued function. We need to choose the two real branches $[W_0(z), W_{-1}(z)]$ and to choose the correct branch according to the value of $\sigma(x)$. The condition in Eq. (17) becomes

$$W_0[Y_{\text{right}}(x_w)] + W_{-1}[-Y_{\text{left}}(x_w)] + 2 = 0. \tag{22}$$

Solving this equation with $Y_{\text{left}}(x_w) = Y_\alpha(x_w)$ or $Y_\beta(x_w)$ (i.e., with the left boundary controlled either by the entrance rate $\alpha$ or by the cargo-swapping rate $\beta$) yields the corresponding location of the shock.

We show an example of a density profile and kymograph for a system with two shocks in Fig. 12(b). We plot a solution for Eq. (22) in the inset of Fig. 12(a). The plateau in the shock location is reached when the entrance rate ($\alpha$) is equal to the density with maximum current in the periodic system $[(1 - v_r)/2]$. As we take $\omega_{A,D} \sim 1/L$ there is a single event (on average) at each time step. Therefore this mechanism has $\sim O(1)$ events after we sample $L$ sites. The mechanism for shocks in the simplified model had $\sim O(1/L)$ events after sampling $L$ sites. Therefore, the shocks are dominated by the LK mechanism even when $\alpha \to 0$.

### B. Diffusive track

We now consider a coupling to a diffusive track, where particles hop symmetrically and do not feel exclusion [see Fig. 4(b) for illustration]. Finite system containing such a diffusive track have been shown to exhibit coexistence of low-density and high-density regions [9,34]. We consider no influx to the diffusive track at the protrusion base (only out-flux), so particles enter this track only by its coupling to the active track. As before we choose the scaling $\omega_{A/D} \sim 1/L$ and the hopping rate in the diffusive track is $D$.

We show kymographs and density profiles of this process in Fig. 13. As we see the system still separates to different parallelograms with different density regions. In Fig. 13(a) we see a behavior similar to the simplified model [compare to Fig. 9 case (c)], where we expect no shock to appear and we find that the diffusive track induces only a small modification. In Fig. 13(b) we present a case where the simplified model still does not exhibit a shock, but the diffusive track is now dominating the dynamics and a discontinuity in the density profile appears. This shock is located between the shocks of a system without inactive particles and entrance rates that correspond to $\alpha$ and $\beta$ in our model [see dashed curves in Fig. 13(b)]. In general the shock location increase as we increase the ratio $\Omega_D/\Omega_A$ or the diffusive hopping rate $D$. Calculations of the density profiles and the resulting phase diagrams for this and the LK models are beyond the scope of this paper.

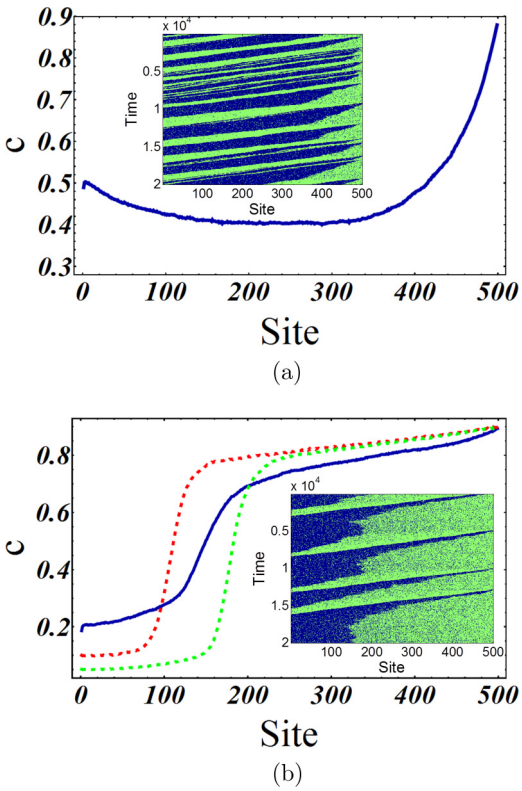


FIG. 13. (Color online) Density profiles and kymographs (insets) for a track coupled to a diffusive track with (a) $\alpha = 0.1, \beta = 0.05, \Omega_A = 0.2, \Omega_D = 0.1, v_r = 0.1, D = 0.5, \Lambda_f = 0.5$; (b) $\alpha = 0.1, \beta = 0.05, \Omega_A = 0.1, \Omega_D = 0.4, v_r = 0.1, D = 2, \Lambda_f = 0.1$. Right and left dashed curves correspond to a system without inactive particles with entrance rates $\alpha$ and $\beta$, respectively. In both figures there is only out-flux from the diffusive track at the protrusion base.

## VI. DISCUSSION AND CONCLUSIONS

Our model is able to reproduce two experimental observations of molecular motors in actin-based cellular protrusions, namely, the finite accumulation length of the motors at the protrusions' tips, and the formation of backward-moving aggregates of motors from the tip to the base. In our model these two phenomena are linked, and both arise from the random process of traffic-jam initiation at the tip, followed by the "relay-race" -like transport of the cargo between the motors. Note, however, that this mechanism is maintaining individual motors near the tip, since only one motor is recycled back to the cytoplasm per traffic jam. Since there are multiple parallel actin tracks inside a real protrusion, we expect the turnover of motors to be more efficient than our one-dimensional model suggests. The effects of such parallel tracks will be explored in a future elaboration of this work.

Since the cargo carried by the motors is often involved in enhancing the actin polymerization at the tip, the length of system may depend on the density at the tip [8,22,23]. While in the current work we considered a fixed geometry, we propose

to investigate the feedback between motors and protrusion length in the future, similar to Refs. [35–37].

From the theoretical point of view we introduce here a model that has several unique features, compared to previous models of molecular motors traffic [34–36,38]: (1) We find that the MFA fails, while it works well in separated domains of the system that are connected through shocks, and (2) we find that while there is a steady-state *average* density, the spatiotemporal behavior of the system is inherently dynamic: a shock can appear in the *average* steady-state density profile, but it undergoes intermittent collapses. We presented a method to calculate the density profiles and phase diagram of a simplified model without attachment and detachment events. Extending the simplified model to include attachment and detachment events, both to an infinite reservoir (LK) and to a diffusive track, we find the same qualitative spatiotemporal structure; i.e., the system evolution separates into well-defined time slices due to the jams. Therefore, we believe that the same calculation method can be applied to the two other models. However, we find that the attachment and detachment processes can dominate and control the position of the shock in the system.

Finally, we can make several qualitative predictions related to the phenomena observed in cellular protrusions. Both the actin polymerization rate ($v_r$) and the influx of motors ($\alpha$) may be modified in experiments, and therefore the phase diagram of Fig. 9 can be explored. We predict that increasing the treadmilling will result in a decrease of the average jam size [Eq. (12)]. The parameters $K_f,\beta$ are controlled by the cargo affinity to the motors: By modifying $\beta$ the system will change its phase according to Fig. 9(a), and through $K_f$ the average size of the jams can be manipulated [Eq. (12)]. The basic mechanism which allows the formation of jams in the model (cargo swapping) implies that motors that have become inactive at the protrusion tip can be reactivated inside the protrusion and not only at the cell cytoplasm [39].

## ACKNOWLEDGMENTS

We gratefully acknowledge funding from the ISF (Grant No. 580/12). This research is made possible in part by the generosity of the Harold Perlman Family. We thank Kirone Mallick and Tridib Sadhu for useful discussions.

## APPENDIX A: RATE OF EFFECTIVE PROCESS

In this section we show that the bidirectional cargo swapping with symmetric rates $\tilde{\beta}$ is equivalent to au-nidirectional process with rate $\beta = \frac{\tilde{\beta}}{1+\tilde{\beta}}$ as depicted in Fig. 1(b).

Effectively particles are getting released from the jam with a rate $r = \tilde{\beta} p_0$ where $p_0$ is the probability there are no particles on the right side of the defect. By writing the probability for $n$ particles on the right side of the defect as $p_n$ (see Fig. 14 for illustration), we have the following equations:

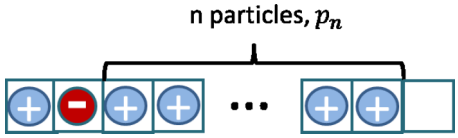


FIG. 14. (Color online) A state with probability $p_n$ has $n$ particles from the right of the defect.

$$\begin{aligned} \dot{p}_0 &= (1+\tilde{\beta})p_1 - \tilde{\beta} p_0, \\ \dot{p}_n &= \tilde{\beta} p_{n-1} + (1+\tilde{\beta})p_{n+1} - (1+2\tilde{\beta})p_n; \quad n > 0. \end{aligned} \tag{A1}$$

Solving these equations at steady state yields

$$p_n = \frac{\tilde{\beta}^n}{(1+\tilde{\beta})^n} p_0. \tag{A2}$$

Combining the result with the normalization $\sum p_n = 1$ we get $p_0 = 1/(1+\tilde{\beta})$, and

$$\beta = r = \tilde{\beta} p_0 = \frac{\tilde{\beta}}{1+\tilde{\beta}}. \tag{A3}$$

Since the system is at steady state the current is spatially constant in the free flow region, and therefore the average density in the HD region is $\beta$. We conclude that

$$c_f = \beta = \frac{\tilde{\beta}}{1+\tilde{\beta}}. \tag{A4}$$

We stress that if we would assume unidirectional reaction, i.e., only the right particle can swap a cargo at a rate $\beta$, we would get the same result [25]. The last important note is that if the system is blocked, such that no motor motion is possible, the cargo would perform a symmetric random walk among the stationary motors.

## APPENDIX B: CONDITIONAL MEANS

We present the results for the conditional means presented in Sec. III. For $x > x_w$:

$$\begin{aligned} \langle x_{v_r i} | a \rangle &= \frac{\beta}{\Lambda_f (1-v_r)(1-\beta)} + 1 - x, \\ \langle x_{v_r i} | b \rangle &= \frac{\beta}{\Lambda_f (1-v_r)(1-\beta)} \\ &\quad - \frac{\exp\left[\frac{\Lambda_f (1-v_r)(1-\beta)}{\beta}(x-1)\right]}{1-\exp\left[\frac{\Lambda_f (1-v_r)(1-\beta)}{\beta}(x-1)\right]}(1-x). \end{aligned} \tag{B1}$$

For $x < x_w$:

$$\langle t_f|A\rangle = L\left[\frac{1}{\Lambda_f(1-v_r)}+\frac{1-\beta}{\beta}-\frac{1-c_-}{c_-}x-\frac{c_--\beta}{c_-\beta}x_w\right],$$

$$\langle x_{1i}|B\rangle = \frac{c_-}{\Lambda_f(1-v_r)(1-c_-)}-\frac{c_--\beta}{\beta(1-c_-)}(1-x_w) + \frac{\frac{c_-(1-\beta)(1-x_w)}{\beta(1-c_-)}\exp\left[\frac{\Lambda_f(1-v_r)(1-\beta)}{\beta}(x_w-1)\right]-\frac{\beta(1-c_-)(1-x)+(c_--\beta)(1-x_w)}{\beta(1-c_-)}\exp\left[\frac{\Lambda_f(1-v_r)(c_--\beta)}{c_-\beta}(x_w-1)+\frac{\Lambda_f(1-v_r)(1-c_-)}{c_-}(x-1)\right]}{\exp\left[\frac{\Lambda_f(1-v_r)(1-\beta)}{\beta}(x_w-1)\right]-\exp\left[\frac{\Lambda_f(1-v_r)(c_--\beta)}{c_-\beta}(x_w-1)\right]\exp\left[\frac{\Lambda_f(1-v_r)(1-c_-)}{c_-}(x-1)\right]},$$

$$\langle x_{v_ri}|C_1\rangle = \frac{\beta}{\Lambda_f(1-v_r)(1-\beta)}+\frac{\frac{\beta(1-c_-)}{v_r(1-v_r-\beta-c_-)}x\exp\left[-\frac{\Lambda_f(1-c_)(1-v_r)(1-\beta)}{v_r(1-v_r-\beta-c_)}\right]-(1-x_w)\exp\left[\frac{\Lambda_f(1-v_r)(1-\beta)}{\beta}(x_w-1)\right]}{\exp\left[-\frac{\Lambda_f(1-c_)(1-v_r)(1-\beta)}{v_r(1-v_r-\beta-c_)}\right]-\exp\left[\frac{\Lambda_f(1-v_r)(1-\beta)}{\beta}(x_w-1)\right]}, \tag{B2}$$

$$\langle x_{v_ri}|C_2\rangle = \frac{\beta}{\Lambda_f(1-v_r)(1-\beta)}-\frac{\beta(1-c_-)}{v_r(1-v_r-\beta-c_-)}\frac{\exp\left[\frac{\Lambda_f(1-v_r)(1-c_-)}{c_-}(x-1)\right]}{1-\exp\left[\frac{\Lambda_f(1-v_r)(1-c_-)}{c_-}(x-1)\right]}.$$

## APPENDIX C: CALCULATION DETAILS FOR DENSITY PROFILES

### 1. Calculation for $x > x_w$

Here we show the details of the density profile calculation. We begin with for $x > x_w$ by calculating the different contributions in Eq. (1). The first contribution is of the $1-v_r$ region, which only arise due to subset $a$, as can be seen in Fig. 7(a):

$$\sum_i t_{v_{ri}} = \sum_{i\in a} t_{v_{ri}} = \sum_{i\in a}\left[t_{f_i}-\frac{(1-x)}{\beta}+(1-x)\right] = N_{1-x<x_{v_r}}\left[\frac{1-\beta}{\beta}\langle x_{v_ri}|a\rangle-\frac{1-\beta}{\beta}(1-x)\right], \tag{C1}$$

where we used result 5 to get from the first to the second row. $N_{1-x<x_{v_r}}$ denote the number of parallelograms with $1-x<x_{v_r}$. Plugging Eq. (B1) we get

$$\sum_i t_{v_{ri}} = N_{1-x<x_{v_r}}\frac{1}{\Lambda_f(1-v_r)}. \tag{C2}$$

We now turn to calculate

$$\sum_i t_{\beta_i} = \sum_{i\in a} t_{\beta_i}+\sum_{i\in b} t_{\beta_i}. \tag{C3}$$

Calculating each term separately:

$$\sum_{i\in a} t_{\beta_i} = \sum_{i\in a}\left(\frac{1}{\beta}-\frac{1}{\beta+v_r}\right)(1-x) = \sum_{i\in a}\frac{v_r}{\beta(\beta+v_r)}(1-x) = N_{1-x<x_{v_r}}\frac{v_r}{\beta(\beta+v_r)}(1-x), \tag{C4}$$

and

$$\sum_{i\in b} t_{\beta_i} = \sum_{i\in a}\frac{v_r}{\beta(\beta+v_r)}x_{v_ri} = N_{1-x>x_{v_r}}\frac{v_r}{\beta(\beta+v_r)}\langle x_{v_r}|b\rangle. \tag{C5}$$

Plugging the conditional mean in the second term and summing the two terms we get

$$\sum_i t_{\beta_i} = N_{1-x<x_{v_r}}\frac{v_r}{\beta(\beta+v_r)}(1-x)+N_{1-x>x_{v_r}}\frac{v_r}{\Lambda_f(1-v_r)(1-\beta)(\beta+v_r)} - N_{1-x>x_{v_r}}\frac{v_r}{\beta(\beta+v_r)}\frac{\exp\left[\frac{\Lambda_f(1-v_r)(1-\beta)}{\beta}(x-1)\right]}{1-\exp\left[\frac{\Lambda_f(1-v_r)(1-\beta)}{\beta}(x-1)\right]}(1-x). \tag{C6}$$

The final term (which is due to the jams) is

$$\sum_i t_{J_i} = \sum_{i\in a} t_{J_i} + \sum_{i\in b} t_{J_i}, \tag{C7}$$

and we use the same steps as before to get

$$\sum_i t_{J_i} = N_{1-x<x_{v_r}} \frac{1-\beta-v_r}{(\beta+v_r)}(1-x) + N_{1-x>x_{v_r}} \frac{\beta(1-\beta-v_r)}{\Lambda_f(1-v_r)(1-\beta)(\beta+v_r)}$$
$$- N_{1-x>x_{v_r}} \frac{1-\beta-v_r}{(\beta+v_r)} \frac{\exp\left[\frac{\Lambda_f(1-v_r)(1-\beta)}{\beta}(x-1)\right]}{1-\exp\left[\frac{\Lambda_f(1-v_r)(1-\beta)}{\beta}(x-1)\right]}(1-x). \tag{C8}$$

Notice that

$$\begin{aligned}\frac{N_{1-x<x_{v_r}}}{N} &= P\left(1-x<x_{v_r}\right)\\ &= \exp\left[\frac{\Lambda_f(1-v_r)(1-\beta)}{\beta}(x-1)\right],\\ \frac{N_{1-x>x_{v_r}}}{N} &= P\left(1-x>x_{v_r}\right)\\ &= 1-\exp\left[\frac{\Lambda_f(1-v_r)(1-\beta)}{\beta}(x-1)\right],\end{aligned} \tag{C9}$$

where $N$ is total number of parallelograms. Relations (C9) are the result of dividing the number of slices where $1-x > x_{v_r}, < x_{v_r}$ with the total number of slices; thus we get the cumulative distribution function of the exponential distribution of $x_{v_r}$. Result (C6) simplifies to

$$\sum_i t_{\beta_i} = N_{1-x>x_{v_r}} \frac{v_r}{\Lambda_f(1-v_r)(1-\beta)(\beta+v_r)}, \tag{C10}$$

and result (C8) simplifies to

$$\sum_i t_{J_i} = N_{1-x>x_{v_r}} \frac{\beta(1-\beta-v_r)}{\Lambda_f(1-v_r)(1-\beta)(\beta+v_r)}. \tag{C11}$$

The denominator in Eq. (1) is $\sum t_{f_i} = N\langle t_f\rangle = N\frac{1}{\Lambda_f(1-v_r)}$. Dividing Eqs. (C2), (C10), and (C11) with this result, summing them and using relations (C9) we get

$$c(x) = \frac{\beta}{\beta+v_r} + \left(1-v_r-\frac{\beta}{\beta+v_r}\right) \times \exp\left[\frac{\Lambda_f(1-v_r)(1-\beta)}{\beta}(x-1)\right]. \tag{C12}$$

### 2. Calculation for $x < x_w$

We now consider $x < x_w$. As before we average over different times slices. The contribution of the $c_-$ density region is

$$\sum_i t_{ci} = \sum_{i\in A} t_{ci} + \sum_{i\in B} t_{ci} + \sum_{i\in C_1} t_{ci}. \tag{C13}$$

Writing the different terms explicitly we get

$$\begin{aligned}\sum_{i\in A} t_{ci} &= N_A \frac{1-v_r-\beta}{c_-(1-v_r-\beta-c_-)}(x_w-x),\\ \sum_{i\in B} t_{ci} &= N_B\left[\frac{v_r}{c_-(c_-+v_r)}\langle x_{1i}|B\rangle - \frac{v_r}{c_-(c_-+v_r)} - \frac{1-\beta}{(c_-+v_r)(1-v_r-\beta-c_-)}x + \frac{1-v_r-\beta}{c_-(1-v_r-\beta-c_-)}x_w\right],\\ \sum_{i\in C_1} t_{ci} &= N_{C_1}\frac{v_r(1-\beta)}{\beta(1-c_-)(c_-+v_r)}\langle x_{v_r i}|C_1\rangle - N_{C_1}\frac{1-\beta}{(c_-+v_r)(1-v_-\beta-c_-)}x.\end{aligned} \tag{C14}$$

$N_A, N_B, N_{C_1}$ denote the number of parallelograms in subsets $A, B, C_1$, respectively. The jam regions give

$$\sum_i t_{Ji} = \sum_{i\in A} t_{Ji} + \sum_{i\in B} t_{Ji} + \sum_{i\in C_1} t_{Ji} + \sum_{i\in C_2} t_{Ji}, \tag{C15}$$

where

$$\begin{aligned}\sum_{i\in A} t_{Ji} &= N_A\frac{1-v_r-\beta}{\beta+v_r}(1-x), \quad \sum_{i\in B} t_{Ji} = N_B\left[\frac{1-v_r-c_-}{c_-+v_r}\langle x_{1i}|B\rangle + \frac{c_--\beta}{(\beta+v_r)(c_-+v_r)}(1-x)\right],\\ \sum_{i\in C_1} t_{Ji} &= N_{C_1}\left[\frac{c_-(1-\beta)(1-v_r-c_-)}{\beta(1-c_-)(c_-+v_r)}\langle x_{v_r i}|C_1\rangle - \frac{c_--\beta}{(c_-+v_r)(\beta+v_r)}x\right],\\ \sum_{i\in C_2} t_{Ji} &= N_{C_2}\frac{1-v_r-\beta}{\beta+v_r}\langle x_{v_r i}|C_2\rangle.\end{aligned} \tag{C16}$$

Getting the contributions also from $\beta$ and $1-v_r$ regions and using the conditional means lead to Eq. (10).

[1] D. Chowdhury, Phys. Rep. **529**, 1 (2013).
[2] A. B. Kolomeisky, J. Phys.: Condens. Matter **25**, 463101 (2013).
[3] T. Chou, K. Mallick, and R. Zia, Rep. Prog. Phys. **74**, 116601 (2011).
[4] P. Mattila and P. Lappalainen, Nat. Rev. Mol. Cell Biol. **9**, 446 (2008).
[5] M. E. Schneider, A. C. Dosé, F. T. Salles, W. Chang, F. L. Erickson, B. Burnside, and B. Kachar, J. Neurosci. **26**, 10243 (2006).
[6] J. Berg and R. Cheney, Nat. Cell Biol. **4**, 246 (2002).
[7] I. Belyantseva, E. Boger, S. Naz, G. Frolenkov, J. Sellers, Z. Ahmed, A. Griffith, and T. Friedman, Nat. Cell Biol. **7**, 148 (2005).
[8] F. Salles, R. Merritt, U. Manor, G. Dougherty, A. Sousa, J. Moore, C. Yengo, A. Dosé, and B. Kachar, Nat. Cell Biol. **11**, 443 (2009).
[9] M. J. Müller, S. Klumpp, and R. Lipowsky, J. Phys.: Condens. Matter **17**, S3839 (2005).
[10] M. Naoz, U. Manor, H. Sakaguchi, B. Kachar, and N. S. Gov, Biophys. J. **95**, 5706 (2008).
[11] P. Zhuravlev, Y. Lan, M. Minakova, and G. Papoian, Proc. Natl. Acad. Sci. USA **109**, 10849 (2012).
[12] A. Parmeggiani, T. Franosch, and E. Frey, Phys. Rev. Lett. **90**, 086601 (2003).
[13] G. Schutz, in *Phase Transitions and Critical Phenomena*, Vol. 19, edited by C. Domb and J. L. Lebowitz (Academic, New York, 2000).
[14] M. Schreckenberg, A. Schadschneider, K. Nagel, and N. Ito, Phys. Rev. E **51**, 2939 (1995).
[15] K. Nishinari, Y. Okada, A. Schadschneider, and D. Chowdhury, Phys. Rev. Lett. **95**, 118101 (2005).
[16] T. Reichenbach, T. Franosch, and E. Frey, Phys. Rev. Lett. **97**, 050603 (2006).
[17] S. Klumpp, Y. Chai, and R. Lipowsky, Phys. Rev. E **78**, 041909 (2008).
[18] I. Pinkoviezky and N. S. Gov, New J. Phys. **15**, 025009 (2013).
[19] I. Pinkoviezky and N. S. Gov, Phys. Rev. E **88**, 022714 (2013).
[20] N. Umeki, H. Jung, T. Sakai, O. Sato, R. Ikebe, and M. Ikebe, Nat. Struct. Mol. Biol. **18**, 783 (2011).
[21] U. Manor, M. Grati, C. M. Yengo, B. Kachar, and N. S. Gov, BioArchitecture **2**, 171 (2012).
[22] H. Tokuo and M. Ikebe, Biochem. Biophys. Res. Commun. **319**, 214 (2004).
[23] U. Manor, A. Disanza, M. Grati, L. Andrade, H. Lin, P. P. Di Fiore, G. Scita, and B. Kachar, Curr. Biol. **21**, 167 (2011).
[24] C. Goldman and E. T. Sena, Physica A **388**, 3455 (2009).
[25] K. Mallick, J. Phys. A **29**, 5375 (1996).
[26] M. Kerber, D. Jacobs, L. Campagnola, B. Dunn, T. Yin, A. Sousa, O. Quintero, and R. Cheney, Curr. Biol. **19**, 967 (2009).
[27] J. A. Spudich, Nature (London) **372**, 515 (1994).
[28] B. Derrida, E. Domany, and D. Mukamel, J. Stat. Phys. **69**, 667 (1992).
[29] A. B. Kolomeisky, G. M. Schütz, E. B. Kolomeisky, and J. P. Straley, J. Phys. A **31**, 6911 (1998).
[30] H. Hinsch and E. Frey, Phys. Rev. Lett. **97**, 095701 (2006).
[31] C. Arita, J. Bouttier, P. L. Krapivsky, and K. Mallick, Phys. Rev. E **88**, 042120 (2013).
[32] A. Parmeggiani, T. Franosch, and E. Frey, Phys. Rev. E **70**, 046101 (2004).
[33] R. Corless, G. Gonnet, D. Hare, D. Jeffrey, and D. Knuth, Adv. Comput. Math. **5**, 329 (1996).
[34] R. Lipowsky, S. Klumpp, and T. M. Nieuwenhuizen, Phys. Rev. Lett. **87**, 108101 (2001).
[35] A. Melbinger, L. Reese, and E. Frey, Phys. Rev. Lett. **108**, 258104 (2012).
[36] K. E. P. Sugden, M. R. Evans, W. C. K. Poon, and N. D. Read, Phys. Rev. E **75**, 031909 (2007).
[37] K. Sugden and M. Evans, J. Stat. Mech. (2007) P11013.
[38] D. Johann, C. Erlenkämper, and K. Kruse, Phys. Rev. Lett. **108**, 258103 (2012).
[39] O. A. Quintero, W. C. Unrath, S. M. Stevens, U. Manor, B. Kachar, and C. M. Yengo, J. Biol. Chem. **288**, 37126 (2013).